38th International Electric Vehicle Symposium and Exhibition (EVS38)
Göteborg, Sweden, June 15-18, 2025

Data-Driven ECM Parameter Update with EIS for Enhanced Onboard SoC Estimation in Lithium-Ion Batteries

Yilei Lin, Hangying Li, Markus Lienkamp
Technical University of Munich (TUM), School of Engineering & Design,
Department of Mobility Systems, Institute of Automotive Technology,
yilei.lin@tum

Executive Summary

Accurate state of charge estimation is vital for the performance and reliability of lithium-ion batteries in electrical vehicles. Traditional onboard methods use equivalent circuit model (ECM) with fixed parameters, which degrade in accuracy over time and varying conditions. Electrochemical impedance spectroscopy (EIS) captures detailed insights into battery states. Leveraging recent hardware advancements, this study proposed two data-driven methods to update ECM parameters using EIS data.
This study introduces two data-driven approaches to dynamically update ECM parameters using over 6,000 EIS measurements. A frequency-relative sensitivity analysis guided model structure selection, and synthetic data were generated to enhance training. The proposed methods include an XGBoost-based structure classifier with a Random Forest (RF) regressor and a physics-constrained 1D-CNN. The XGBoost-RF model demonstrated high classification accuracy and low estimation errors, even with limited data. Meanwhile, the 1D-CNN, though computationally heavier and more data-dependent, showed strong adaptability in complex scenarios and achieved comparable accuracy when trained on augmented datasets.
Keywords: Electric Vehicles, AI - Artificial intelligence for EVs, Batteries, Battery Management System

1 Introduction

Accurate state of charge (SoC) estimation is essential for reliable range prediction, efficient energy management, and safe operation of electric vehicles. Among various SoC estimation methods, model-based approaches are the most widely adopted [1]. Specifically, equivalent circuit model (ECM) has gained popularity for its acceptable modeling accuracy, easy offline parameterization, and suitability for real-time implementation [2]. However, ECM parameters are sensitive to a range of operating conditions, including SoC, state of health (SoH), and temperature [3, 4]. Traditionally, look-up tables have been used to capture these dependencies, but this approach requires extensive experimental data to cover the full operational range [5]. As the battery ages, this method can become inaccurate, as earlier characterizations may no longer reflect the battery's current state [5]. To address these challenges, online recursive parameter estimation methods, such as recursive least squares and adaptive filters, have been explored. However, these approaches often encounter numerical stability issues and require complex tuning, complicating their onboard implementation [6–9].
Electrochemical impedance spectroscopy (EIS) has traditionally been used in laboratories to analyze electrochemical processes in the battery and is well-established for offline parameter identification in ECM [10]. Recent studies also demonstrated its potential for SoC estimation in laboratory settings [11–14]. However, certain limitations arise in onboard applications. Specifically, the time required

for conducting EIS measurements and the challenge of finding appropriate operational windows for data collection conflict with the demand for continuous, real-time SoC monitoring in onboard systems. Nevertheless, EIS still offers significant potential for enhancing onboard SoC estimation accuracy when integrated with ECM-based methods. By providing insights into battery degradation and electrochemical behavior, EIS data can be used to dynamically adjust ECM parameters, preserving model accuracy under diverse conditions and as the battery ages. This hybrid approach leverages the strengths of both EIS and ECM-based estimation methods.

In this study, aging experiments on 12 cells were conducted to collect EIS data under various operating conditions (different SoC, SoH, and temperatures) simulating real-world electric vehicle usage. Based on the collected EIS datasets, two data-driven ECM parameter update methods are proposed and their performance is evaluated.

The structure of this paper is as follows: section 2 introduces the experimental setup used for this paper, which includes the design of the experiments for the aging and the characterization process. Section 3 presents the ECM fitting process to generate labels for model training. A frequency-relative ECM parameter sensitivity analysis was conducted and based on those results, three simplified ECM structures were proposed and fitted. In section 4, the proposed eXtreme Gradient Boosting (XGBoost)-Random Forest (RF) and 1-Dimensional Convolutional Neural Network (1D-CNN) frameworks are introduced, and their performance are evaluated. Section 5 provides a summary of the study, discusses its limitations, and outlines potential directions for future research. A schematic workflow is shown in Fig. 1.

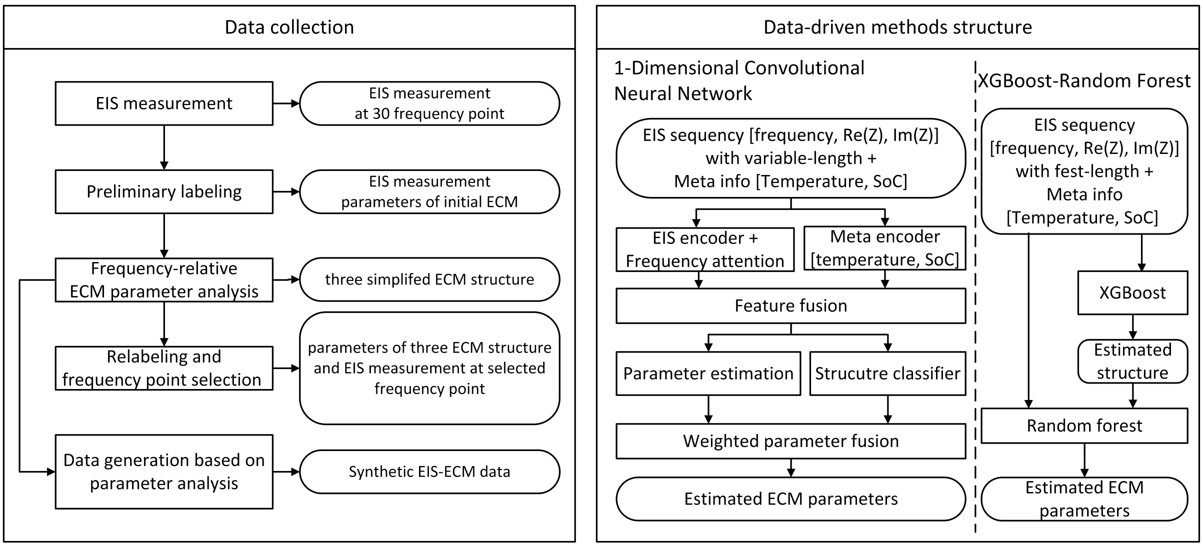

Figure 1: Workflow of the proposed data-driven ECM parameterization framework

2 Experimental setup

This section introduces the experimental protocol for the aging experiments. In this study, 12 cylindrical Panasonic NCR18650PF cells with a nominal capacity of 2.9 Ah were used. All cells underwent five charge–discharge cycles for activation, followed by initial characterization. This characterization included measurements of cell capacity and impedance across various SoC, ranging from 0% to 100% in 5% increments, and at a temperature of 10, 25 and 40 °C. The cells were grouped according to the initial results of the characterization, ensuring that the capacity variation within each group did not exceed 1.0%. The complete experimental structure and detailed setup are introduced in the following sections.

2.1 Aging processes

A variety of charge-discharge combinations were employed to study the relationship between EIS data and operating conditions (temperature, SoC, and SoH). In this work, continuous-cycle aging processes were conducted to accelerate the battery's progression toward the end of life. The 12 Panasonic 18650 cells were divided into four groups (A-D), each subjected to a unique cycling profile, as detailed in Table 1. Groups A and B were assigned to standard aging protocols and each included 4 cells. Groups C and D were categorized as extreme accelerated aging mode, and each included 2 cells.

The cycling processes were conducted using the BioLogic BCS-815 system at an ambient temperature of 25 °C, maintained by a Binder KB115 E4 climate chamber. Cells from Groups A and B were characterized every 25 cycles, while fast-charged cells (Groups C and D) were tested every 10 cycles to capture accelerated degradation effects. The aging process was designed to conclude when the SoH reached 80%. As of the current reporting stage, the aging process is still ongoing, with most cells exhibiting a SoH of approximately 93%.

Group number	Charge profile	Discharge profile	Battery cell ID
A	0.5 C	Highway profile	A1 – A4
B	0.5 C	Commuter profile	B1 – B4
C	2 C	Highway profile	C1 – C2
D	2 C	Commuter profile	D1 – D2

Table 1: Battery aging experiment configuration

2.2 Characterization procedure

After the aging procedure, the cells were subjected to a characterization process. The capacity of each cell was measured to calculate the SoH, and EIS measurements were performed at various SoC (same as in the initial characterization) to analyze changes in ECM parameters under different operating conditions.

EIS measurements were conducted over a frequency range of 10 mHz to 10 kHz with a current amplitude of 100 mA, collecting six frequency points per decade. To ensure more stable impedance data, a relaxation period of 20 min was scheduled after reaching the target SoC prior to each EIS measurement. The three temperature levels were controlled using a Binder KB115 E4 climate chamber, with ambient temperature deviation maintained within ±2 °C. After reaching the target temperature, a 2-hour resting period was applied to ensure uniform temperature distribution within the cell before EIS measurements commenced.

The overall experimental workflow is illustrated in Fig. 2, where the blue box denotes the aging process and the orange box indicates the characterization process.

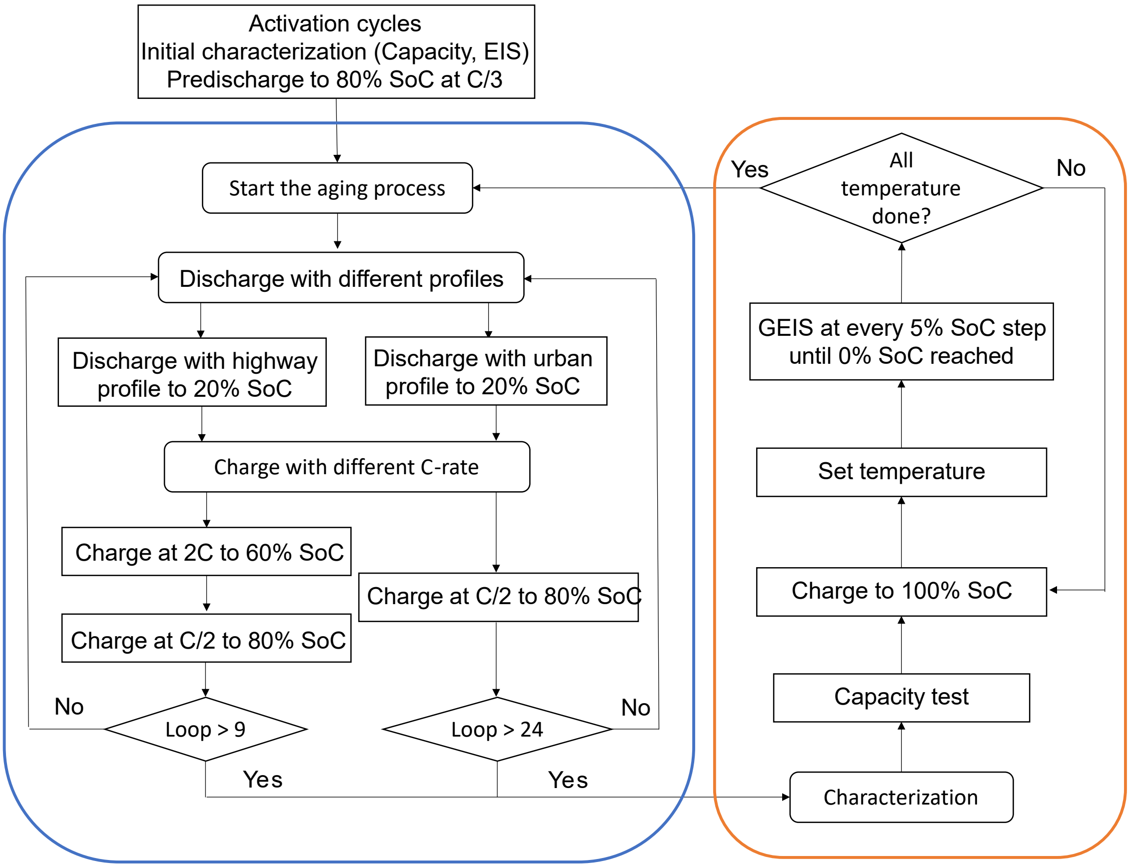

Figure 2: Schematic of the experimental data collection

3 Data processing and labeling

As a low-signal technique, EIS measurement requires the system to be time-invariant, linear and causal [15]. However, due to various sources of interference, such as measurement noise, the measurement may not strictly satisfy these assumptions [16]. To ensure data reliability, the linear Kramers–Kronig (KK) validation method proposed by Boukamp was employed to assess physical consistency [17], and measurements violating plausibility criteria were excluded. In total, 6083 valid EIS datasets were obtained. A Savitzky-Golay smoothing filter was applied to balance noise suppression and spectral fidelity.
The resulting smoothed EIS data were initially fitted using an ECM with the structure illustrated in Fig. 3. However, since the form of the impedance spectra varies under different battery operating conditions, the universal ECM structure was found to be suboptimal for some cases. In addition, the complexity of this model is relatively high, which could pose a challenge for onboard implementation. To improve fitting performance, a frequency-relative ECM parameter sensitivity analysis was performed based on the initial fit. Based on this analysis, three optimal simplified ECM structures were selected for different conditions, with each EIS spectrum assigned its most suitable model structure. Finally, the EIS data were re-fitted using nonlinear least-squares optimization with their respective optimal structures. The resulting ECM parameters were used as labels for the subsequent training process.

3.1 Frequency-relative ECM parameter sensitivity analysis

Electrochemical processes within the battery occur over a broad spectrum of timescales, ranging from milliseconds to several days or longer. To capture such complex dynamics, ECM topologies with different numbers of parallel resistance-capacitor (RC) branches have been proposed. With advancements in EIS technology, fractional-order models have attracted increasing attention due to their improved accuracy in simulating complex battery behavior [18]. A typical fractional-order model is illustrated in Fig. 3, consisting of a series inductance (L_0) and ohmic resistance (R_0), followed by two parallel branches: one representing the solid electrolyte interphase (SEI) layer using a resistor and capacitor network (R_{SEI}, C_{SEI}), and the other representing the charge transfer and double layer effects through a resistor and constant phase element (CPE) (R_{CT}, CPE_{DL}) [19]. To account for the sloped behavior often observed in the low-frequency region of EIS spectra, an additional parallel branch composed of a Warburg element and a diffusion-related capacitance (W_o, C_{diff}) is included to characterize ion diffusion processes. However, the operating conditions of electric vehicles are highly dynamic, and the time available for onboard EIS measurements is limited. The inclusion of multiple parallel branches significantly increases the computational burden of parameter identification, making complex ECM structures impractical for real-time applications in EVs [20]. As a result, many existing studies adopt simplified topologies containing one or two RC or R-CPE branches, often omitting explicit modeling of the diffusion process [18–20].

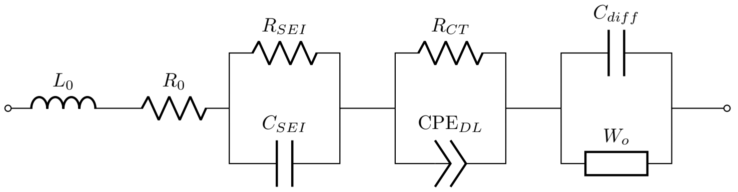

Figure 3: Complete ECM structure for modeling battery impedance over the entire frequency range

To investigate the evolving impedance behavior under various operating conditions, Fig. 4 presents the Nyquist plots at different temperatures (10°, 25°, and 40°) and SoC levels. At low temperatures (10°) and extreme SoC conditions (0% and 100%), two distinct semicircles—typically corresponding to the SEI layer and the charge transfer process, double layer effect can be clearly observed. In contrast, at higher temperatures or moderate SoC levels, the two semicircles begin to overlap, complicating the separation of the underlying electrochemical mechanisms. Consequently, it becomes necessary to employ multiple ECM structures, incorporating either single or dual RC/R-CPE parallel branches, to accurately fit the EIS data across varying operating conditions.
To further determine the appropriate ECM structure and its corresponding EIS frequency sampling range for each impedance spectrum, a perturbation-based frequency-domain analysis was performed to identify regions predominantly influenced by diffusion-related dynamics. These regions were subsequently excluded from the impedance dataset to ensure that the simplified models maintain accurate parameter estimation while remaining robust to the omission of low-frequency processes. Beginning with the initial circuit topology, each parameter was independently perturbed in increments of 1%, while keeping the remaining parameters fixed. At each perturbation step, the corresponding impedance $Z_{\text{pert}}(f)$ was calculated and compared against the baseline $Z_{\text{ref}}(f)$ across frequencies up to 1 kHz. The frequency-resolved relative residuals in the real and imaginary components were computed as:

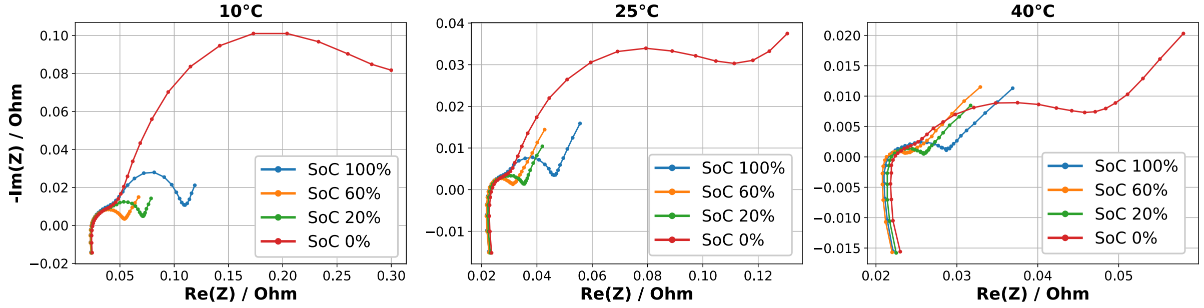

Figure 4: Parameters distribution over SoC

$$\varepsilon_{\text{real}}(f_k) = \left| \frac{\mathrm{Re}(Z_{\text{pert}}(f_k)) - \mathrm{Re}(Z_{\text{ref}}(f_k))}{\mathrm{Re}(Z_{\text{ref}}(f_k))} \right| \times 100\% \tag{1}$$

$$\varepsilon_{\text{imag}}(f_k) = \left| \frac{\mathrm{Im}(Z_{\text{pert}}(f_k)) - \mathrm{Im}(Z_{\text{ref}}(f_k))}{\mathrm{Im}(Z_{\text{ref}}(f_k))} \right| \times 100\% \tag{2}$$

The perturbation process was terminated once the residual in either component exceeded 5% at any frequency point [21]:

$$\max_f \left(\varepsilon_{\text{real}}(f), \varepsilon_{\text{imag}}(f) \right) > 5\% \tag{3}$$

When the perturbation applied to an ECM parameter reaches a level such that the residual in either the real or imaginary part of the generated EIS data exceeds 5% compared to the measured EIS, the ratio between the perturbed and original values of that ECM parameter is recorded as the scale threshold for the corresponding parameter.

3.2 Results of the sensitivity analysis

To illustrate the results, the EIS data measured at 100% SoH, 100% SoC, and 25 °C was selected as a representative case. As shown in Fig. 5a, the perturbation in R_0 resulted in a relatively large residual in the real part of the impedance across the entire frequency range, indicating that R_0 has a broad influence on the impedance spectrum. Perturbations in other components led to varying degrees of deviations in the real and imaginary parts of the impedance spectrum. Notably, the Warburg element W_o primarily affected the impedance at frequencies below 1 Hz (Fig. 5h-i), while the diffusion capacitance C_{diff} exhibited noticeable influence starting around 10 Hz (Fig. 5g). C_{diff} predominantly governing the transition region between charge transfer and pure diffusion processes, and its effect on the EIS curve can be compensated with CPE_{DL}. L_0 primarily influences the impedance response at high frequencies and reflects parasitic effects. As it does not originate from the intrinsic behavior of the battery, it is typically disregarded [21]. Based on these findings, the low-frequency portion of the EIS spectrum below 1 Hz can be excluded without significantly compromising fitting accuracy. This allows the circuit structure to be simplified by removing both the L_0 inductance and the C_{diff}–W_o branch, as shown in Fig. 6(b). As shown in Fig. 4, under high temperatures or at moderate SoC levels, only a single semicircle appeared, suggesting that SEI, double layer effect and charge transfer processes merged due to accelerated electrochemical kinetics. An alternative circuit topology representing combined SEI, charge transfer and double layer effects with a parallel R–CPE branch, as shown in Fig. 6c, was adopted for those cases.
As shown in Fig. 7, at very low SoC levels, the high-frequency semicircle in the EIS spectrum became increasingly difficult to model accurately using circuit b (Figure. 6b). In order to obtain a better ECM fit, the SEI capacitance (C_{SEI}) was replaced with a CPE, leading to the structure shown in Fig. 6a.
Based on the above analysis, a SoC- and temperature-dependent multi-structure modeling framework was developed, in which three distinct ECM topologies were proposed to accommodate varying operating conditions. Corresponding frequency sampling ranges were selected for each condition and are summarized in Table 2.
Using the newly defined ECM structures and the corresponding truncated EIS datasets with non-uniform frequency sampling, least-squares fitting was performed to extract the ECM parameters, which serve as labels for the training process.

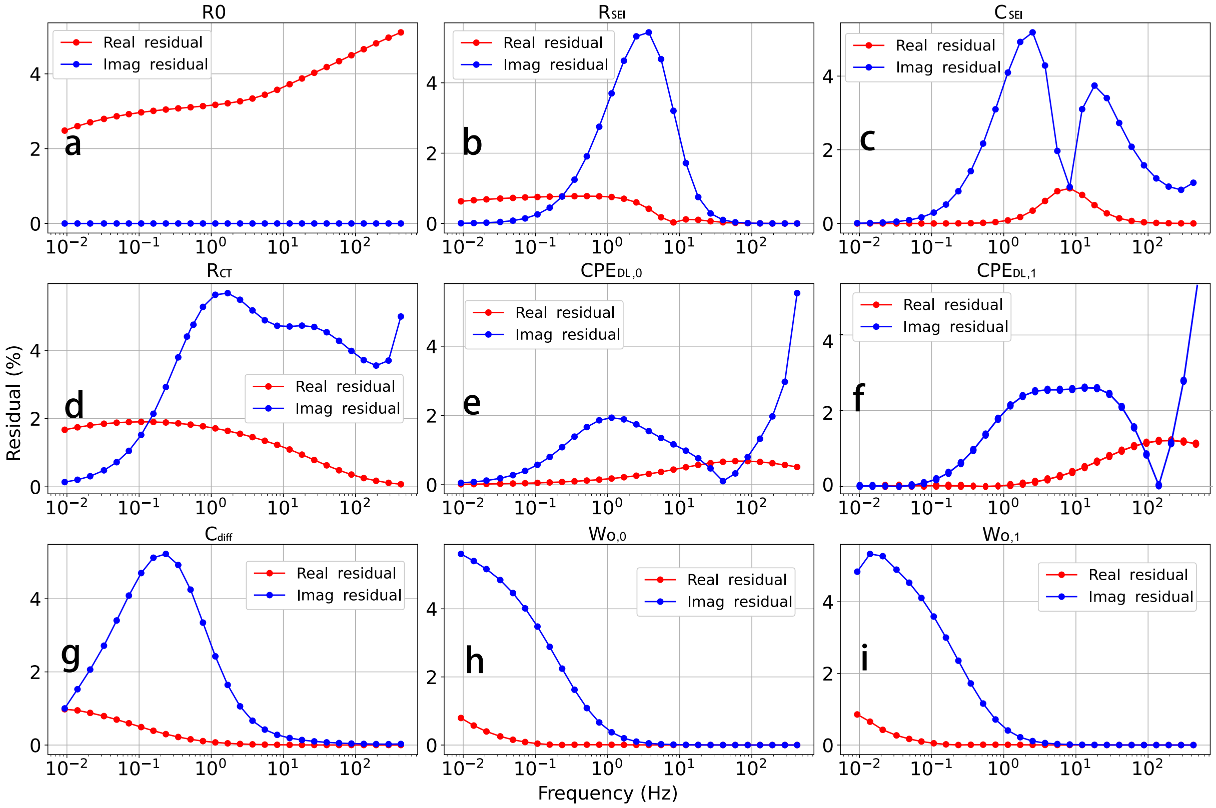

Figure 5: Frequency-resolved residuals at perturbation thresholds for each ECM parameter at 100% SoC, and 25 °C

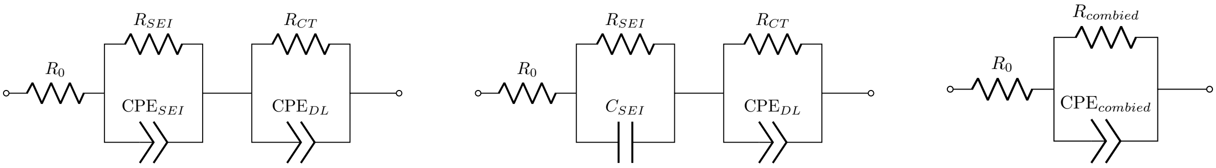

(a) Circuit a: Diffusion branch removed; C_{SEI} replaced with a CPE

(b) Circuit b: Diffusion branch removed

(c) Circuit c: Multi effects branch

Figure 6: ECM structures under different simplification levels

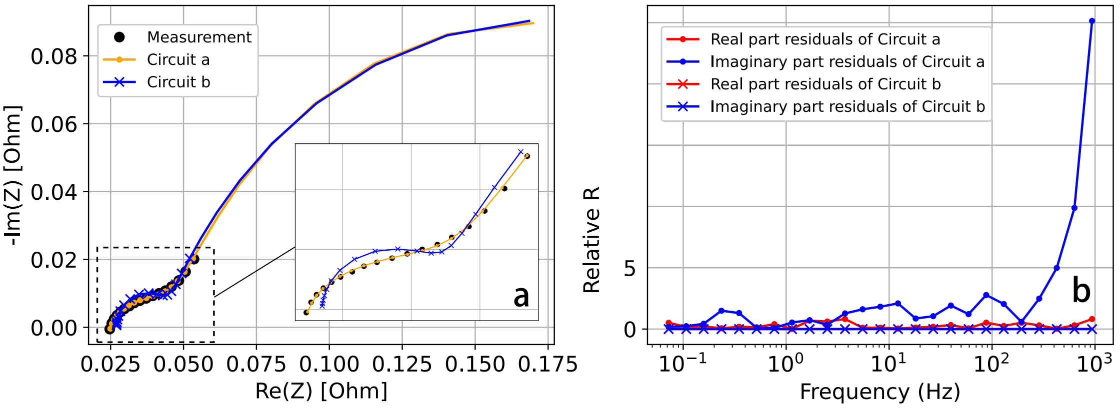

Figure 7: Fitting performance comparison of two ECM structures at 5% SoC and 10°C. Fig. a: Nyquist plot showing the measurement and model fittings; Fig. b: Relative residuals versus frequency.

Table 2: Selected ECM topologies and frequency ranges under different temperatures and SoC conditions.

Temperature in °C	SoC range in SoC	Selected circuit	Frequency range in Hz
10	95–100	Circuit a	0.3–1000
	85–90	Circuit b	1.2–1000
	50–80	Circuit b	2–1000
	35–45	Circuit b	2–1000
	25–30	Circuit b	1–1000
	15–20	Circuit b	0.3–1000
	0–10	Circuit a	0.05–1000
25	95–100	Circuit b	1–1000
	85–90	Circuit b	5–1000
	35–80	Circuit c	5–1000
	25–30	Circuit b	5–1000
	20	Circuit b	2–1000
	15	Circuit a	1–1000
	5–10	Circuit a	0.3–1000
	0	Circuit a	0.1–1000
40	90–100	Circuit b	5–500
	65–85	Circuit c	10–500
	55–60	Circuit c	20–500
	25–50	Circuit c	15–500
	15–20	Circuit b	5–500
	5–10	Circuit b	1–500
	0	Circuit b	0.5–500

Table 3: Scale thresholds of ECM parameters at 25°C for 100% and 20% SoC levels (threshold defined at 5% EIS residual)

Condition	R_0	R_{SEI}	C_{SEI}	R_{DL}	$\mathrm{CPE}_{\mathrm{DL},0}$	$\mathrm{CPE}_{\mathrm{DL},1}$
100% SoC, 25°C	1.06	1.10	1.24	1.05	1.04	1.02
20% SoC, 25°C	1.06	1.29	1.53	1.04	1.03	0.01

As shown, the variation in parameter values remains relatively small and generally does not exceed 10% when the residual is constrained to be below 5%. Notably, R_{SEI} and C_{SEI} exhibit larger deviations under certain conditions. Therefore, these two parameters are incorporated as additional constraint conditions when generating synthetic data, a strategy also discussed in Ref. [21].

4 Data-driven frameworks

In this work, two preliminary modeling frameworks are proposed based on a balance between model simplicity and adaptability to varying operating conditions. The first framework employs XGBoost as a classifier to select the ECM structure and RF as a regressor to estimate the parameters. This structure is relatively simple, interpretable, and suitable for small to moderate-sized datasets. The second framework is based on a 1D-CNN, which offers higher generalization capability, particularly under large-scale data scenarios.

4.1 XGBoost-RF based model

XGBoost is an open-source implementation of the gradient boosting framework, featuring gradient-based optimization, and is thus capable of handling high-dimensional feature spaces [22].As another ensemble learning method, the RF is widely adopted for regression problems. In RF, a large number of decision trees are independently trained on randomly resampled subsets of the original dataset, and their outputs are averaged to produce the final prediction. Owing to tree independence and feature randomness, RF exhibits strong resilience against overfitting, robustness to noisy inputs, and good generalization even with relatively small datasets.

In this work, the regression task focuses on parameterizing ECM models with varying structures. Accordingly, three separate RF regressors are developed, each dedicated to a specific ECM structure. Due to differences in the available frequency sampling across experiments, the number of frequency points varies between samples. To ensure uniform input dimensions, the EIS data with different lengths were interpolated prior to model input, resulting in a fixed set of 30 frequency points for each sample. The appropriate structure is identified using an XGBoost-based classifier, which then directs the input to the corresponding RF module, as illustrated in Fig. 8 in the left side. Each RF model is trained to learn only the parameters relevant to its assigned ECM structure, resulting in improved accuracy and reduced overfitting.

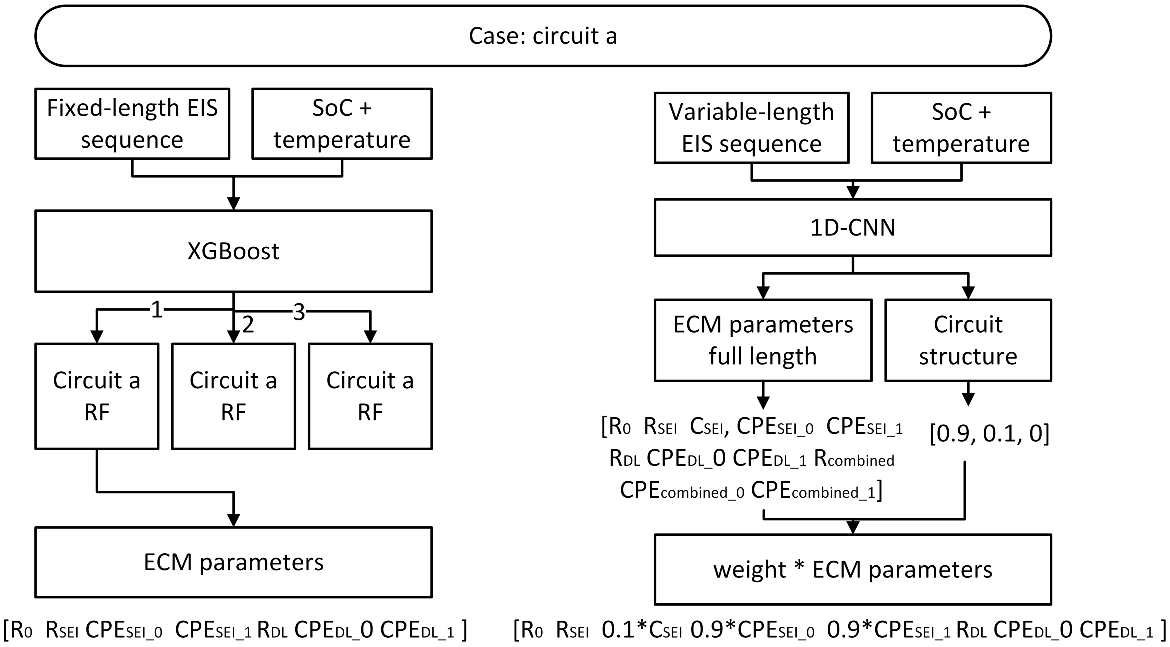

Figure 8: Inference workflow of 1D-CNN and XGBoost-RF models for circuit a

Hyperparameter settings for all models are summarized in Table 4.

Table 4: Summary of Hyperparameter Settings for All Models

Model	Hyperparameter	Value / Range
XGBoost	Max Depth	3, 5, 7 (random search)
	Learning Rate	0.01–0.1 (random search)
	Number of Estimators	100, 200 (random search)
	Subsample Ratio	0.8, 1.0 (random search)
Random Forest	Max Depth	20 (fixed)
	Number of Estimators	100 (fixed)
1D-CNN	Learning Rate	4.22×10^{-5}
	Batch Size	32
	Dropout Rate	0.22
	Weight Decay	1.24×10^{-5}
	Number of Epochs	100

4.2 Structure-aware and physics-constrained 1D-CNN framework

Although the XGBoost-RF framework enables fast and accurate ECM parameterization under limited data conditions, its performance relies heavily on feature engineering and shows limited generalization to unseen operating scenarios. To address these challenges, this work further proposes a structure-aware and physics-constrained neural network architecture, aiming to achieve robust and scalable ECM parameter estimation directly from EIS measurements.

The input layer consists of two components: (i)variable-length EIS sequences of variable lengths, where each sequence contains measurements of real and imaginary impedance components at a set of frequency points. To enable uniform batch processing, EIS sequences are zero-padded to the maximum sequence length and standardized prior to input; (ii) scalar meta-information including normalized temperature and SoC, which provides contextual information on operating conditions and facilitate more accurate modeling of impedance responses under varying thermal and electrochemical environments.

A one-dimensional convolutional encoder with hierarchical layers is employed to extract localized spectral features. Frequency information is incorporated via a frequency-aware attention mechanism, enabling the model to dynamically assign importance weights to different spectral regions. Simultaneously, temperature and SoC features are processed through a fully connected network and fused into the latent representation, enhancing model generalization across operating conditions.

The output of the encoder is fed into a joint feature space, from which two branches emerge: one for ECM structure classification and another for parameter regression. Specifically, a structure classifier predicts a probability vector $\boldsymbol{\alpha} \in \mathbb{R}^3$, corresponding to three predefined ECM structures. Parallel to this, three structure-specific regression heads estimate the parameter vector

$$\mathbf{p} = [R_0,\, R_{\text{SEI}},\, C_{\text{SEI}},\, \text{CPE}_{\text{SEI},0},\, \text{CPE}_{\text{SEI},1},\, R_{\text{CT}},\, \text{CPE}_{\text{DL},0},\, \text{CPE}_{\text{DL},1},\, R_{\text{combined}},\, \text{CPE}_{\text{combined},0},\, \text{CPE}_{\text{combined},1}]^\top,$$

In order to avoid greater deviation caused by hard selection, a soft fusion of the outputs is performed according to the structure probabilities:

$$\hat{\mathbf{p}} = \sum_{k=1}^{3} \alpha_k \cdot \hat{\mathbf{p}}^{(k)},$$

where $\hat{\mathbf{p}}^{(k)}$ denotes the prediction from the k-th head.

The training objective combines two terms: (i) a complex nonlinear least squares (CNLS) loss $\mathcal{L}_{\text{CNLS}}$ minimizing the discrepancy between the reconstructed and measured impedance curves based on predicted parameters; and (ii) a cross-entropy loss $\mathcal{L}_{\text{classification}}$ for structure prediction:

$$\mathcal{L}_{\text{total}} = \lambda_{\text{reg}} \mathcal{L}_{\text{CNLS}} + \lambda_{\text{cls}} \mathcal{L}_{\text{classification}},$$

where λ_{reg} and λ_{cls} are balancing coefficients. In this work λ_{reg} is 0.7, λ_{cls} is 0.3.

For each sample i, the CNLS loss is defined as:

$$\begin{aligned}\mathcal{L}_{\text{CNLS}}^{(i)} = \frac{1}{S_i} \sum_{k=1}^{S_i} \Bigg[& \Big(\text{Re}\left(\hat{Z}(f_k; \mathbf{p}_i, L_{0,i}, \mathcal{S}_i)\right) - \text{Re}\left(Z_{\text{meas},i}(f_k)\right)\Big)^2 \\ & + \Big(\text{Im}\left(\hat{Z}(f_k; \mathbf{p}_i, L_{0,i}, \mathcal{S}_i)\right) - \text{Im}\left(Z_{\text{meas},i}(f_k)\right)\Big)^2 \Bigg]\end{aligned} \tag{4}$$

where:

- $\mathbf{p}_i$ denotes the estimated ECM parameter vector,
- $L_{0,i}$ is the estimated inductance,
- $\mathcal{S}_i$ is the selected circuit structure,
- S_i is the number of frequency points for sample i.

The final CNLS loss across the batch is computed as:

$$\mathcal{L}_{\text{CNLS}} = \frac{1}{B} \sum_{i=1}^{B} \mathcal{L}_{\text{CNLS}}^{(i)} \tag{5}$$

where B is the batch size.

4.3 Results and comparison

To establish a rigorous foundation for evaluating the proposed machine learning approaches, both experimentally measured and synthetically generated EIS datasets were used to evaluate the proposed frameworks. Initially, 10% of the entire measured dataset was reserved as a test set, while the remaining 90% was split into training and validation sets in a 4:1 ratio. For experiments involving synthetic data, given the objective of assessing the model's capability to parameterize ECMs based on real measurements, synthetic samples were excluded from the validation and test sets. The measured data were evenly divided into training, validation, and test subsets, while synthetic samples, along with an additional 2000 real measurements, were used for model training.

On the measurement-only dataset comprising 6083 EIS samples, the XGBoost-RF framework achieved 97.37% classification accuracy and low regression errors, demonstrating robust performance under data-limited conditions. In comparison, the 1D-CNN model exhibited slightly higher classification accuracy but showed increased RMSE and MAE, likely due to its larger capacity and the limited experimental dataset failing to support effective feature learning.

The use of combined synthetic and partial experimental EIS data for training resulted in high predictive accuracy in both structure classification and parameter regression. The overall classification accuracy of XGBoost-RF framework reached 97.70%. As detailed in Table 5, the classifier correctly recognized the majority of ECM structures. A closer inspection of the confusion matrix reveals that circuit a was perfectly classified, suggesting that its features are clearly distinguishable from those of the other two structures. However, a small portion of circuit b samples were misclassified as either circuit a or circuit c, and a limited number of circuit c samples were predicted as circuit b. This behavior indicates partial feature overlap between circuits b and c, which may introduce ambiguity in structure identification and merits further investigation.

Table 5: Confusion matrix for structure classification of XGBoost-RF framework

True \ Estimated	Circuit a	Circuit b	Circuit c
Circuit a	180	0	0
Circuit b	5	547	10
Circuit c	0	13	462

In the 1D-CNN framework, classification accuracy improved slightly, with corresponding decreases in RMSE and MAE. Most misclassifications occurred between circuit b and the other circuits, which can be attributed to the inherent ambiguity in some EIS profiles where different circuit topologies yield similar impedance responses. Since the ultimate objective is accurate impedance reconstruction and parameter inference, and the 1D-CNN framework employs soft-fusion for structure fusion, classification errors do not necessarily propagate to parameter estimation errors. These results demonstrate the flexibility of the neural model in handling complex or ambiguous measurement scenarios.

Furthermore, a loss function combining the CNLS fitting term with parameter estimation error was employed to guide the training of the 1D-CNN. While the inclusion of CNLS loss improved physical consistency and helped address the imbalance introduced by differences in parameter magnitudes, it also introduced substantial computational overhead. In certain cases, parameter amplification during denormalization led to numerical instability during impedance reconstruction, causing divergence in the training loss. A masking strategy was applied to exclude physically implausible estimations, and the reported 1D-CNN performance metrics were derived from this physically filtered subset. Additionally, the best results were selected from multiple training, validation, and test runs. Due to the large number of excluded samples, the statistical validity of the reported metrics remains uncertain. This issue will be investigated in future work.

The Evaluation metrics are summarized in Table 6.

Table 6: Evaluation results of proposed Machine Learning Methods on Different Datasets

Parameter	XGBoost-RF		1D-CNN	
	Measured	Synthetic	Measured	Synthetic
Classification accuracy (%)	97.37	97.70	98.85	99.92
MAE	0.5637	0.4331	3.1295	3.0561
RMSE (%)	4.7419	2.4737	7.5512	6.9401
R^2	0.5557	0.8563	0.4983	0.5152

5 Summary and limits

Overall, these results indicate that XGBoost-RF are well-suited for applications with limited data and constrained computational resources, offering strong performance with relatively simple architectures. In contrast, deep learning models such as the 1D-CNN provide higher modeling flexibility and scalability. Future research will focus on improving the efficiency of CNN-based parameter estimation. Conventional loss functions often face difficulties in multi-parameter regression tasks due to large disparities in parameter magnitudes. Although the CNLS loss improves physical consistency, it introduces considerable computational overhead. A potential solution is to decompose the frequency domain and apply localized CNLS losses within sub-bands, which may reduce computational demands while preserving physical fidelity. In addition, extending the concept of soft-fusion—currently employed in the CNN framework—to ensemble models like XGBoost-RF could be a promising strategy to mitigate the impact of occasional classification errors. This could enhance the robustness and adaptability of tree-based models in more complex or ambiguous real-world environments.

Acknowledgments

This work was supported by the project “LiBRA” under grant number “DIE-2305-0003//DIE0512/02” from the Bayerisches Verbundforschungsprogramm (BayVFP). We gratefully acknowledge the financial support provided by the Bavarian State Ministry for Economic Affairs, Regional Development and Energy.

References

[1] R. Xiong, J. Cao, Q. Yu, H. He, and F. Sun, “Critical Review on the Battery State of Charge Estimation Methods for Electric Vehicles,” *IEEE Access*, vol. 6, pp. 1832–1843, 2018. [Online]. Available: http://ieeexplore.ieee.org/document/8168251/

[2] J. Meng, G. Luo, M. Ricco, M. Swierczynski, D.-I. Stroe, and R. Teodorescu, “Overview of Lithium-Ion Battery Modeling Methods for State-of-Charge Estimation in Electrical Vehicles,” *Applied Sciences*, vol. 8, no. 5, p. 659, Apr. 2018. [Online]. Available: https://www.mdpi.com/2076-3417/8/5/659

[3] W. Widanage, A. Barai, G. Chouchelamane, K. Uddin, A. McGordon, J. Marco, and P. Jennings, “Design and use of multisine signals for Li-ion battery equivalent circuit modelling. Part 1: Signal design,” *Journal of Power Sources*, vol. 324, pp. 70–78, Aug. 2016. [Online]. Available: https://linkinghub.elsevier.com/retrieve/pii/S0378775316305511

[4] ——, “Design and use of multisine signals for Li-ion battery equivalent circuit modelling. Part 2: Model estimation,” *Journal of Power Sources*, vol. 324, pp. 61–69, Aug. 2016. [Online]. Available: https://linkinghub.elsevier.com/retrieve/pii/S037877531630550X

[5] C. Zhang, W. Allafi, Q. Dinh, P. Ascencio, and J. Marco, “Online estimation of battery equivalent circuit model parameters and state of charge using decoupled least squares technique,” *Energy*, vol. 142, pp. 678–688, Jan. 2018. [Online]. Available: https://linkinghub.elsevier.com/retrieve/pii/S0360544217317127

[6] Y. Li, J. Chen, and F. Lan, “Enhanced online model identification and state of charge estimation for lithium-ion battery under noise corrupted measurements by bias compensation recursive least squares,” *Journal of Power Sources*, vol. 456, p. 227984, Apr. 2020. [Online]. Available: https://linkinghub.elsevier.com/retrieve/pii/S0378775320302871

[7] K. Saleem, K. Mehran, and Z. Ali, “Online reduced complexity parameter estimation technique for equivalent circuit model of lithium-ion battery,” *Electric Power Systems Research*, vol. 185, p. 106356, Aug. 2020. [Online]. Available: https://linkinghub.elsevier.com/retrieve/pii/S0378779620301620

[8] X. Guo, L. Kang, Y. Yao, Z. Huang, and W. Li, “Joint Estimation of the Electric Vehicle Power Battery State of Charge Based on the Least Squares Method and the Kalman Filter Algorithm,” *Energies*, vol. 9, no. 2, p. 100, Feb. 2016. [Online]. Available: https://www.mdpi.com/1996-1073/9/2/100

[9] X. Zhang, Y. Wang, D. Yang, and Z. Chen, “An on-line estimation of battery pack parameters and state-of-charge using dual filters based on pack model,” *Energy*, vol. 115, pp. 219–229, Nov. 2016. [Online]. Available: https://linkinghub.elsevier.com/retrieve/pii/S0360544216312312

[10] D. Andre, “Characterization of high-power lithium-ion batteries by electrochemical impedance spectroscopy. II: Modelling,” *Journal of Power Sources*, 2011.

[11] Q.-K. Wang, Y.-J. He, J.-N. Shen, X.-S. Hu, and Z.-F. Ma, “State of Charge-Dependent Polynomial Equivalent Circuit Modeling for Electrochemical Impedance Spectroscopy of Lithium-Ion Batteries,” *IEEE Transactions on Power Electronics*, vol. 33, no. 10, pp. 8449–8460, Oct. 2018. [Online]. Available: https://ieeexplore.ieee.org/document/8166792/

[12] I. Babaeiyazdi, A. Rezaei-Zare, and S. Shokrzadeh, “State of charge prediction of EV Li-ion batteries using EIS: A machine learning approach,” *Energy*, vol. 223, p. 120116, May 2021. [Online]. Available: https://linkinghub.elsevier.com/retrieve/pii/S0360544221003650

[13] D. Sun, X. Yu, C. Wang, C. Zhang, R. Huang, Q. Zhou, T. Amietszajew, and R. Bhagat, “State of charge estimation for lithium-ion battery based on an Intelligent Adaptive Extended Kalman Filter with improved noise estimator,” *Energy*, vol. 214, p. 119025, Jan. 2021. [Online]. Available: https://linkinghub.elsevier.com/retrieve/pii/S0360544220321320

[14] N. Chen, P. Zhang, J. Dai, and W. Gui, “Estimating the State-of-Charge of Lithium-Ion Battery Using an H-Infinity Observer Based on Electrochemical Impedance Model,” *IEEE Access*, vol. 8, pp. 26 872–26 884, 2020. [Online]. Available: https://ieeexplore.ieee.org/document/8978682/

[15] N. Meddings *et al.*, “Application of electrochemical impedance spectroscopy to commercial li-ion cells: A review,” *Journal of Power Sources*, vol. 480, p. 228742, 2020.

[16] S. D. Talian *et al.*, “Impedance spectroscopy applied to lithium battery materials: Good practices in measurements and analyses,” *Energy Storage Materials*, vol. 69, p. 103413, 2024.

[17] B. A. Boukamp *et al.*, “A linear kronig-kramers transform test for immittance data validation,” *Journal of The Electrochemical Society*, vol. 142, pp. 1885–1894, 1995.

[18] R. Xiong, J. Tian, W. Shen, and F. Sun, “A novel fractional order model for state of charge estimation in lithium ion batteries,” *IEEE Transactions on Vehicular Technology*, vol. 68, no. 5, pp. 4130–4139, 2019.

[19] J. Peng, J. Meng, J. Wu, Z. Deng, M. Lin, S. Mao, and D.-I. Stroe, “A comprehensive overview and comparison of parameter benchmark methods for lithium-ion battery application,” *Journal of Energy Storage*, vol. 71, p. 108197, 7 2023. [Online]. Available: https://doi.org/10.1016/j.est.2023.108197

[20] W. Merrouche, B. Lekouaghet, E. Bouguenna, and Y. Himeur, “Parameter estimation of ECM model for Li-Ion battery using the weighted mean of vectors algorithm,” *Journal of Energy Storage*, vol. 76, p. 109891, 11 2023. [Online]. Available: https://doi.org/10.1016/j.est.2023.109891

[21] A. Zulueta, E. Zulueta, J. Olarte, U. Fernandez-Gamiz, J. M. Lopez-Guede, and S. Etxeberria, “Electrochemical Impedance spectrum equivalent circuit parameter identification using a deep learning technique,” *Electronics*, vol. 12, no. 24, p. 5038, 12 2023. [Online]. Available: https://doi.org/10.3390/electronics12245038

[22] T. Chen and C. Guestrin, “Xgboost: A scalable tree boosting system,” in *Proceedings of the 22nd ACM SIGKDD International Conference on Knowledge Discovery and Data Mining*, ser. KDD ’16. New York, NY, USA: Association for Computing Machinery, 2016, p. 785–794. [Online]. Available: https://doi.org/10.1145/2939672.2939785

Presenter Biography

Yilei Lin received her bachelor’s degree in Mechanical Engineering, specializing in Automotive Technology, from the Technical University of Dresden (TUD) in 2019. She completed her Master’s in Mechanical Engineering with a concentration in Mechatronics and Robotics at the Technical University of Munich (TUM) in 2023. Currently, she is pursuing a Ph.D. at TUM’s Institute of Automotive Technology, where her research is dedicated to advancing the application of onboard Electrochemical Impedance Spectroscopy (EIS) for electric vehicles.